

## OBSERVATIONS OF MKN 421 WITH THE MAGIC TELESCOPE

J. ALBERT<sup>A</sup>, E. ALIU<sup>B</sup>, H. ANDERHUB<sup>C</sup>, P. ANTORANZ<sup>D</sup>, A. ARMADA<sup>B</sup>, M. ASENSIO<sup>D</sup>, C. BAIXERAS<sup>E</sup>, J. A. BARRIO<sup>D</sup>, H. BARTKO<sup>G</sup>, D. BASTIERI<sup>H</sup>, J. BECKER<sup>F</sup>, W. BEDNAREK<sup>J</sup>, K. BERGER<sup>A</sup>, C. BIGONGIARI<sup>H</sup>, A. BILAND<sup>C</sup>, R. K. BOCK<sup>G,H</sup>, P. BORDAS<sup>U</sup>, V. BOSCH-RAMON<sup>U</sup>, T. BRETZ<sup>A</sup>, I. BRITVITCH<sup>C</sup>, M. CAMARA<sup>D</sup>, E. CARMONA<sup>G</sup>, A. CHILINGARIAN<sup>K</sup>, S. CIPRINI<sup>L</sup>, J. A. COARASA<sup>G</sup>, S. COMMICHAU<sup>C</sup>, J. L. CONTRERAS<sup>D</sup>, J. CORTINA<sup>B</sup>, V. CURTEF<sup>F</sup>, V. DANIELYAN<sup>K</sup>, F. DAZZI<sup>H</sup>, A. DE ANGELIS<sup>I</sup>, R. DE LOS REYES<sup>P</sup>, B. DE LOTTO<sup>I</sup>, E. DOMINGO-SANTAMARÍA<sup>B</sup>, D. DORNER<sup>A</sup>, M. DORO<sup>H</sup>, M. ERRANDO<sup>B</sup>, M. FAGIOLINI<sup>O</sup>, D. FERENC<sup>N</sup>, E. FERNÁNDEZ<sup>B</sup>, R. FIRPO<sup>B</sup>, J. FLIX<sup>B</sup>, M. V. FONSECA<sup>D</sup>, L. FONT<sup>E</sup>, M. FUCHS<sup>G</sup>, N. GALANTE<sup>G</sup>, M. GARCZARCYK<sup>G</sup>, M. GAUGH<sup>H</sup>, M. GILLER<sup>J</sup>, F. GOEBEL<sup>G</sup>, D. HAKOBYAN<sup>K</sup>, M. HAYASHIDA<sup>G</sup>, T. HENGSTEBECK<sup>M</sup>, D. HÖHNE<sup>A</sup>, J. HOSE<sup>G</sup>, C. C. HSU<sup>G</sup>, P. JACON<sup>J</sup>, T. JOGLER<sup>G</sup>, O. KALEKIN<sup>M</sup>, R. KOSYRA<sup>G</sup>, D. KRANICH<sup>C</sup>, R. KRITZER<sup>A</sup>, M. LAATIAOUI<sup>G</sup>, A. LAILLE<sup>N</sup>, P. LIEBING<sup>G</sup>, E. LINDFORS<sup>L</sup>, S. LOMBARDI<sup>H</sup>, F. LONGO<sup>P</sup>, J. LÓPEZ<sup>B</sup>, M. LÓPEZ<sup>D</sup>, E. LORENZ<sup>C,G</sup>, P. MAJUMDAR<sup>G</sup>, G. MANEVA<sup>Q</sup>, K. MANNHEIM<sup>A</sup>, O. MANSUTTI<sup>I</sup>, M. MARIOTTI<sup>H</sup>, M. MARTÍNEZ<sup>B</sup>, D. MAZIN<sup>G,\*</sup>, C. MERCK<sup>G</sup>, M. MEUCCI<sup>O</sup>, M. MEYER<sup>A</sup>, J. M. MIRANDA<sup>D</sup>, R. MIRZOYAN<sup>G</sup>, S. MIZOBUCHI<sup>G</sup>, A. MORALEJO<sup>B</sup>, K. NILSSON<sup>L</sup>, J. NINKOVIĆ<sup>G</sup>, E. OÑA-WILHELMI<sup>B</sup>, R. ORDUÑA<sup>E</sup>, N. OTTE<sup>G</sup>, I. OYA<sup>D</sup>, D. PANEQUE<sup>G</sup>, R. PAOLETTI<sup>O</sup>, J. M. PAREDES<sup>U</sup>, M. PASANEN<sup>L</sup>, D. PASCOLI<sup>H</sup>, F. PAUSS<sup>C</sup>, R. PEGNA<sup>O</sup>, M. PERSIC<sup>L,R</sup>, L. PERUZZO<sup>H</sup>, A. PICCIOLI<sup>O</sup>, M. POLLER<sup>A</sup>, E. PRANDINI<sup>H</sup>, A. RAYMERS<sup>K</sup>, W. RHODE<sup>F</sup>, M. RIBÓ<sup>U</sup>, J. RICO<sup>B</sup>, M. RISSI<sup>C</sup>, A. ROBERT<sup>E</sup>, S. RÜGAMER<sup>A</sup>, A. SAGGION<sup>H</sup>, A. SÁNCHEZ<sup>E</sup>, P. SARTORI<sup>H</sup>, V. SCALZOTTO<sup>H</sup>, V. SCAPIN<sup>H</sup>, R. SCHMITT<sup>A</sup>, T. SCHWEIZER<sup>G</sup>, M. SHAYDUK<sup>M,G</sup>, K. SHINOZAKI<sup>G</sup>, S. N. SHORE<sup>S</sup>, N. SIDRO<sup>B</sup>, A. SILLANPÄÄ<sup>L</sup>, D. SOBCZYNSKA<sup>J</sup>, A. STAMERRA<sup>O</sup>, L. S. STARK<sup>C</sup>, L. TAKALO<sup>L</sup>, P. TEMNIKOV<sup>Q</sup>, D. TESCARO<sup>B</sup>, M. TESHIMA<sup>G</sup>, N. TONELLO<sup>G</sup>, A. TORRES<sup>E</sup>, D. F. TORRES<sup>B,T</sup>, N. TURINI<sup>O</sup>, H. VANKOV<sup>Q</sup>, V. VITALE<sup>I</sup>, R. M. WAGNER<sup>G</sup>, T. WIBIG<sup>J</sup>, W. WITTEK<sup>G</sup>, R. ZANIN<sup>H</sup>, J. ZAPATERO<sup>E</sup>

*Draft version November 5, 2007*

### ABSTRACT

The MAGIC telescope took data of very high energy  $\gamma$ -ray emission from the blazar Markarian 421 (Mkn 421) between November 2004 and April 2005. We present a combined analysis of data samples recorded under different observational conditions, down to  $\gamma$ -ray energies of 100 GeV. The flux was found to vary between 0.5 – 2 Crab units (integrated above 200 GeV), considered a low state when compared to known data. Although the flux varied on a day-by-day basis, no short-term variability was observed, although there is some indication that not all nights are in an equally quiescent state. The results at higher energies were found to be consistent with previous observations. A clear correlation is observed between  $\gamma$ -rays and X-rays fluxes, whereas no significant correlation between  $\gamma$ -rays and optical data is seen. The spectral energy distribution between 100 GeV and 3 TeV shows a clear deviation from a power law, more clearly and at lower flux than previous observations at higher energies. The deviation persists after correcting for the effect of attenuation by the extragalactic background light, and most likely is source-inherent. There is a rather clear indication of an inverse Compton peak around 100 GeV. The spectral energy distribution of Mkn 421 can be fitted by a one-zone synchrotron self-compton model suggesting once again a leptonic origin of the very high energy  $\gamma$ -ray emission from this blazar.

*Subject headings:* gamma rays: observations, BL Lacertae objects: individual (Mkn 421)

### 1. INTRODUCTION

Mkn 421 (redshift  $z = 0.030$ ) is the closest known and, along with Mkn 501, the best studied TeV  $\gamma$ -ray emitting blazar. It was the first extragalactic source detected in the TeV energy range using imaging atmospheric Cherenkov telescopes (IACTs) (Punch et al. 1992; Petry et al. 1996). Mkn 421 is currently the source with the fastest observed flux variations among TeV  $\gamma$ -ray emitters. So far it has shown flux variations larger than one order of magnitude, and occasional flux doubling times as short as 15 min (Gaidos et al. 1996; Aharonian et al. 2002). Variations in the hardness of the TeV  $\gamma$ -ray spectrum during flares were reported by several groups (e.g. Krennrich et al. (2002); Aharonian et al. (2005)). Simultaneous observations in the X-ray and GeV-TeV bands show strong evidence for flux correlation (Krawczynski et al. 2001; Błażejowski et al. 2005).

<sup>U</sup> Universitat de Barcelona, E-08028 Barcelona, Spain  
\* correspondence: D. Mazin, mazin@mppmu.mpg.de

<sup>A</sup> Universität Würzburg, D-97074 Würzburg, Germany  
<sup>B</sup> Institut de Física d'Altes Energies, Edifici Cn., E-08193 Bellaterra (Barcelona), Spain  
<sup>C</sup> ETH Zurich, CH-8093 Switzerland  
<sup>D</sup> Universidad Complutense, E-28040 Madrid, Spain  
<sup>E</sup> Universitat Autònoma de Barcelona, E-08193 Bellaterra, Spain  
<sup>F</sup> Universität Dortmund, D-44227 Dortmund, Germany  
<sup>G</sup> Max-Planck-Institut für Physik, D-80805 München, Germany  
<sup>H</sup> Università di Padova and INFN, I-35131 Padova, Italy  
<sup>I</sup> Università di Udine, and INFN Trieste, I-33100 Udine, Italy  
<sup>J</sup> University of Łódź, PL-90236 Lodz, Poland  
<sup>K</sup> Yerevan Physics Institute, AM-375036 Yerevan, Armenia  
<sup>L</sup> Tuorla Observatory, Turku University, FI-21500 Piikkiö, Finland  
<sup>M</sup> Humboldt-Universität zu Berlin, D-12489 Berlin, Germany  
<sup>N</sup> University of California, Davis, CA-95616-8677, USA  
<sup>O</sup> Università di Siena, and INFN Pisa, I-53100 Siena, Italy  
<sup>P</sup> Università di Trieste, and INFN Trieste, I-34100 Trieste, Italy  
<sup>Q</sup> Institute for Nuclear Research and Nuclear Energy, BG-1784 Sofia, Bulgaria  
<sup>R</sup> INAF/Osservatorio Astronomico and INFN Trieste, I-34131 Trieste, Italy  
<sup>S</sup> Università di Pisa, and INFN Pisa, I-56126 Pisa, Italy  
<sup>T</sup> Institut de Ciències de l'Espai (CSIC-IEEC), E-08193 Bellaterra (Barcelona), Spain

Mkn 421 has been detected and studied in all accessible wavelengths of the electromagnetic spectrum from radio waves to very high energy (VHE)  $\gamma$ -rays. The overall spectral energy distribution (SED) shows a typical two bump structure with the first peak in the keV energy range and the second maximum at GeV-TeV energies. The SED is commonly interpreted as beamed, non-thermal emission of synchrotron and inverse-Compton radiation from ultrarelativistic electrons, accelerated by shocks moving along the jets at relativistic bulk speed. Simple one-zone synchrotron-self-Compton (SSC) models (e.g. Coppi (1992); Costamante & Ghisellini (2002)) describe the observational results satisfactorily well. However, hadronic models (Mannheim et al. 1996; Mücke et al. 2003) can explain the observed features, too. A way to distinguish between the different emission models is to determine the position of the second peak in the SED, using simultaneous time-resolved data over a broad energy range through multiwavelegth campaigns. This requires providing data in the as yet unexplored gap in the SED.

The MAGIC telescope (Major Atmospheric Gamma Imaging Cherenkov telescope; see Lorenz (2004)), located on the Canary Island La Palma (2200 m asl, 28°45'N, 17°54'W), completed its commissioning phase in early fall 2004. MAGIC is currently the largest IACT, with a 17 m diameter tessellated reflector dish consisting of 964  $0.5 \times 0.5$  m<sup>2</sup> diamond-milled aluminium mirrors. Together with the current configuration of the MAGIC camera with the trigger region of 2.0 degrees diameter (Cortina et al. 2005), this results in a trigger collection area for  $\gamma$ -rays of the order of  $10^5$  m<sup>2</sup>, increasing with the zenith angle of the observation. Presently the accessible trigger energy range spans from 50-60 GeV (at small zenith angles) up to tens of TeV. The MAGIC telescope is focused to 10 km distance – the most likely position for a 50 GeV air shower. The accuracy in reconstructing the direction of incoming  $\gamma$ -rays on an event by event basis, hereafter  $\gamma$  point spread function (PSF), is about 0.1 degrees, slightly depending on the analysis.

The first physics observations in winter 2004/05 and in spring 2005 included observations of the well established TeV blazar Mkn 421. In total, 19 nights of data were taken on this source, the observation times per night ranging from 30 minutes up to 4 hours. Here we present the results from these observations, covering the energy range from 100 GeV to several TeV. We first describe the data set and analysis techniques in section 2. In section 3, we present the results and, finally, in section 4, we compare our results with other observations and interpret them in terms of different models.

## 2. OBSERVATIONS AND DATA ANALYSIS

The Mkn 421 data were taken between November 2004 and April 2005, and divided into four samples, for reasons given below. Data taken before and after February 2005 were treated separately, due to changes in the telescope hardware. Most of the data were taken at small zenith angles ( $ZA < 30^\circ$ ), i.e. at a low trigger energy threshold. However, observations made during 1.5 hours in a common campaign with the H.E.S.S. telescope system (Mazin et al. 2005) in December 2004 were taken at  $42^\circ < ZA < 55^\circ$ . There were also different observational modes: the standard mode for MAGIC is the

ON-OFF mode, with equal time given to tracking the source in the center of the camera (ON), and tracking a sky region near the source but with the source outside the field of view (OFF). This provides a robust estimate of the background. In our observations, we considered the  $\gamma$ -ray signal from Mkn 421 to be strong enough to obviate OFF observations, and we estimated the background level from the ON data (see below). In April 2005, part of the data were taken in the wobble mode (Daum et al. 1997). In this mode, two sky directions, opposite and  $0.4^\circ$  off the source, were tracked alternately for 20 minutes each, which provides a simultaneous measurement of signal and background. In the wobble mode there is *a priori* no need for additional OFF data.

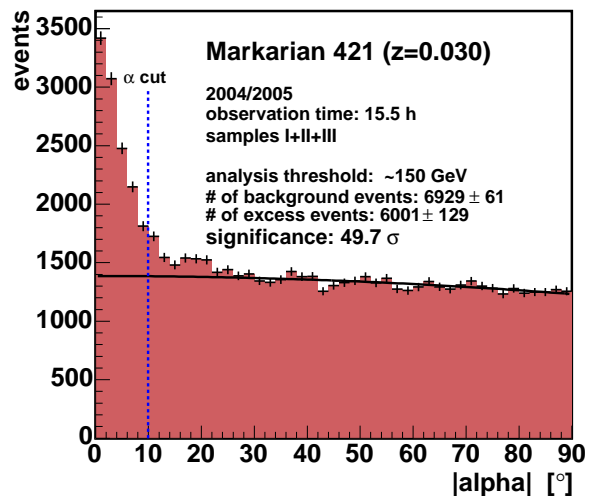


FIG. 1.—  $\alpha$  distribution for the combined data samples I+II+III with  $E_{thresh} = 150$  GeV. A vertical line indicates the  $\alpha$  cut used to extract excess events. The black parabola is a fit to the  $\alpha$  distribution between 30 and 90 degrees and is used to estimate the background level between 0 and 10 degrees.

The observation criteria and some important parameters of the four data samples are summarized in Table 1. For each data sample a separate Monte-Carlo (MC) set of  $\gamma$  events was simulated (CORSIKA version 6.023, Knapp & Heck (2004); Majumdar et al. (2005)), taking into account the zenith angle of observation, the observational mode, and the hardware setup of the telescope. The full data set corresponds to 29.0 hours ON-source observation time. Runs with problems in the hardware or with unusual trigger rates were rejected in order to ensure a stable performance and good atmospheric conditions. After removing these runs, the remaining observation time was 25.6 h.

For calibration, image cleaning, cut optimization, and energy reconstruction the standard analysis techniques of the MAGIC telescope (Bretz 2005; Wagner et al. 2005; Gaug et al. 2005) were applied as shortly described below. The calibration of the raw data from the MAGIC camera uses a system consisting of fast and powerful LED pulsers emitting at three different wavelengths with variable light intensity. Absolute calibration is obtained by comparing the signal of the pixels with the one obtained from a carefully calibrated PIN diode, and is cross-

TABLE 1  
RESULTS OF THE MKN 421 DATA USING THE *Alpha* APPROACH (SEE TEXT FOR DETAILS). SAMPLES I+II WERE RECORDED IN NOVEMBER 2004 - JANUARY 2005, WHILE SAMPLES III+IV WERE TAKEN IN APRIL 2005.

sample	on time	ZA range [°]	mode	$E_{th,r}$ [GeV]	$N_{on}$	$N_{off}$	$N_{excess}$	sigma
I	4.63 h	9.3 - 31.2	ON	150	3761	$1878 \pm 32$	$1883 \pm 69$	29.3
II	1.53 h	42.4 - 55.0	ON	260	1086	$674 \pm 25$	$413 \pm 41$	10.1
III	9.30 h	9.2 - 27.5	ON	150	8083	$4360 \pm 49$	$3723 \pm 102$	38.9
IV	10.12 h	9.4 - 32.4	wobble	150	7740	$4532 \pm 67$	$3208 \pm 111$	29.1

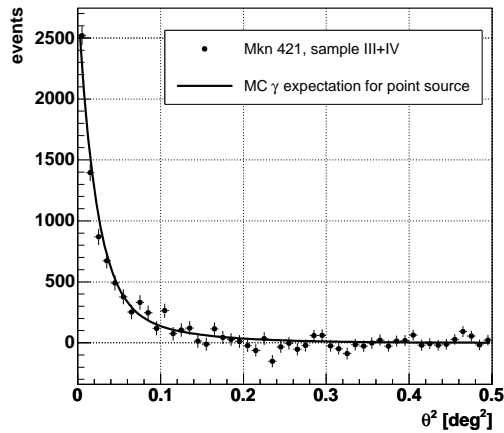


FIG. 2.—  $\theta^2$  distribution for the combined data samples III+IV with  $E_{thresh} = 150$  GeV after background subtraction. The black line is the MC- $\gamma$  expectation for a point source.

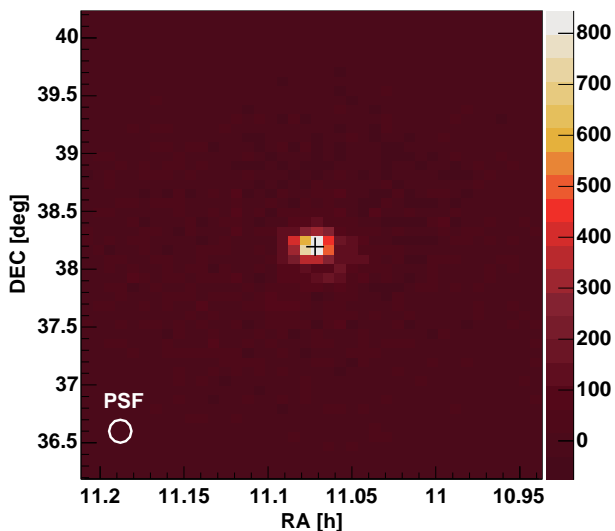


FIG. 3.— Sky map of excess events in the region of Mkn 421 for samples III+IV using the *Disp* method (Domingo-Santamaría et al. 2005). The black cross indicates the reconstructed source position. Note that the vertical scale is in units of [events /  $(0.05 \times 0.05 \text{ deg}^2)$ ].

checked by analysing muon rings. The time resolution of the read-out system has been measured to be about 700 ps for Cherenkov light flashes of 10 photo-electrons (ph.el.) per pixel, reaching 200 ps at 100 ph.el. Calibration events are taken at 50 Hz, interlaced with normal

data, using an external calibration trigger.

The calibrated images are cleaned using so-called tail cuts: pixels are retained only if their reconstructed charge signals are larger than 10 ph.el. ('core pixels') or if their charges are larger than 5 ph. el. and they have at least one neighboring core pixel. The camera images are then reduced to image parameters as in (Hillas 1985), adding parameters describing the intensity concentration and asymmetry.

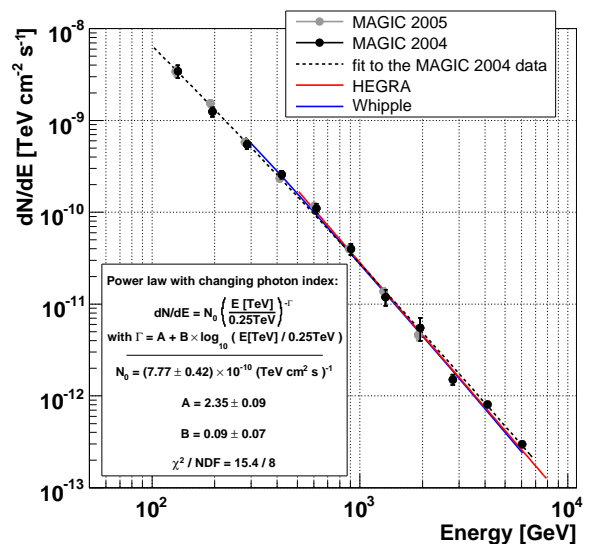


FIG. 4.— Differential energy distribution of the Crab Nebula data sample from 2004 (black circles) and 2005 (grey circles) as measured by MAGIC (Wagner et al. 2005). A fit by power law with a changing photon index to the MAGIC 2004 data is shown by the dashed black line. The analytical form of the fit and the fit parameters are listed in the inlay. Whipple data (solid blue line, Hillas et al. (1998)) and HEGRA data (solid red line, Aharonian et al. (2004)) are shown for comparison.

For  $\gamma$ /hadron separation a multidimensional classification technique based on the Random Forest (RF) method (Breiman 2001; Bock et al. 2004) was used. The RF method uses training data (randomly chosen data events and Monte Carlo  $\gamma$ s, representing background and signal) to find a set of classification trees in the space of image parameters. Multiple trees are combined to form a generalized predictor by taking the mean classification from all trees. The predictor, called hadronness, spans a range between 0 and 1, and characterizes the event images being less or more hadron-like.

In our analysis, classical image shape parameters like *Width*, *Length*, *Dist* and *Size* were used as input parameters. The cuts in hadronness for the  $\gamma$ /hadron separation

ration were trained for each data set separately, and were then chosen such that the overall cut efficiency for MC  $\gamma$  events remained about 50%. The corresponding hadron suppression is about 90-99%, improving with increasing *Size* of the events.

A critical variable not used in the RF classification tree is *Alpha*, the angle between the major image axis and the line connecting the center of gravity of the image with the source position in the camera plane. In stand-alone IACTs, *Alpha* is commonly used, after all previously noted cuts, to extract the  $\gamma$  signal from the data, and to estimate the level of background. For a point source, the *Alpha* distribution of the  $\gamma$ -like events is expected to peak at low values of *Alpha*, whereas for background events the distribution should be flat or slowly varying with *Alpha*.

In the case of our ON-mode data, the background remaining after  $\gamma$ /hadron separation was estimated from the *Alpha* distribution by performing a second order polynomial fit (without linear term) in the range between  $30^\circ$  and  $90^\circ$  where no contribution from  $\gamma$  events is expected (see Fig. 1). The signal was then determined as the number of observed events in the range  $Alpha < Alpha_0$  exceeding the fit extrapolated to small *Alpha*, where  $Alpha_0$  is energy dependent and has a typical value of  $15^\circ$ . The significance of an excess is then calculated according to Eq. 17 in Li & Ma (1983).

In the wobble mode, the ON (*source*) data are defined by calculating image parameters with respect to the source position, whereas OFF data are obtained from the same events but with image parameters calculated with respect to the position on the opposite side of the camera, the *antisource* position. In order to avoid an unwanted contribution from  $\gamma$ -events in the OFF sample and to guarantee the statistical independence between the ON and the OFF samples in the signal region, the following procedure is applied: events with  $Alpha_{source} < Alpha_0$  (with  $Alpha_{source}$  calculated with respect to the source position) are excluded from the OFF sample, and events with  $Alpha_{antisource} < Alpha_0$  (with  $Alpha_{antisource}$  calculated with respect to the antisource position) are excluded from the ON sample. This cut assures that the *Alpha* distributions for ON and OFF events are statistically independent for  $Alpha < Alpha_0$ . The *Alpha* approach was used to determine the excess events for all four data sets (Table 1).

As an alternative to this classical approach using *Alpha*, the so-called  $\theta^2$  approach can be applied, an approach more common for the analysis of data from a system of IACTs like HEGRA or H.E.S.S. The angle  $\theta$  denotes the angular distance between the expected source position and the reconstructed origin of the initial  $\gamma$ -ray. Since for a single IACT the angle  $\theta$  can not be reconstructed directly, the so-called *Disp* method (Fomin et al. 1994; Lessard et al. 2001; Domingo-Santamaría et al. 2005) was used to determine the source position in the camera plane, using position-independent image shape parameters. The number of excess events is then determined as the difference between the  $\theta^2$  distributions for the source and background, respectively, similar to the *Alpha* approach. The background-subtracted  $\theta^2$  distribution for samples III and IV is shown in Fig. 2. The average background was estimated from the wobble data themselves, by exclud-

ing the sector of the camera affected by the presence of the strong source. The solid line in Fig. 2 indicates the expectation from MC- $\gamma$  events for a point source. Computing  $\theta^2$  also permits to produce sky maps in which for every  $\gamma$ -ray candidate an origin in the sky is assigned (see Fig. 3). Note that our signal analysis relies on the *Alpha* approach throughout.

These conservative analysis methods are known to produce reliable results for energies above 100 GeV. The energy regime below 100 GeV will require additional studies, in particular concerning the background rejection. Thus, for our analyzed sample the *Size* parameter (total amount of light of the image and in first order proportional to the energy) was required to be above 150 photoelectrons.

The energy estimation was performed using again the Random Forest technique, based on the image parameters of a MC  $\gamma$  sample. This sample is statistically independent of the one used for the training of the  $\gamma$ /hadron separation cuts. Prior to the training of the energy estimation, loose (high-acceptance) cuts in hadronness and *Alpha* were applied to avoid a possible bias caused by outlier  $\gamma$  events.

The energy thresholds of the individual analyses (as given in Table 1) are defined as the peak in the differential energy distribution of the MC- $\gamma$  events after all cuts. Our analyses showed that we were able to extract excess events with energies  $\sim 50$  GeV lower than the corresponding peak value.

The spectrum of the number of excess events in bins of true energy is determined from the spectrum in the estimated energy by an unfolding procedure. This procedure corrects for the finite energy resolution and for biases in the energy estimation. The unfolding program package used in MAGIC allows unfolding with a variety of methods (Anykeyev et al. (1991)), which differ in the way regularization is implemented. Unfolding results are only accepted if the results from the different methods are consistent with each other and if some criteria are satisfied concerning the regularization strength, the size of the noise component and the  $\chi^2$  value. The latter is a measure of the agreement between the expected “measured” spectrum from the unfolded spectrum and the actually measured spectrum. The unfolding result presented in this analysis was obtained with an iterative method, as described in Bertero (1989).

To demonstrate the quality of the applied analysis and the good agreement with previous measurements by other experiments, we show in Fig. 4 the differential energy spectrum of the Crab Nebula data (“standard candle” of VHE  $\gamma$ -ray astronomy). The data were taken in 2004 and 2005 with observation conditions and telescope performance similar to those of the Mkn 421 data. Additional publications describing details of the calibration methods and the data analysis are in preparation.

### 3. RESULTS

#### 3.1. *The signal*

During the entire observation period, Mkn 421 was found to be in a low flux state compared with existing data (around 1 Crab unit for a flux integrated above 200 GeV), but resulting in a clear signal in all four data samples. Fig. 1 shows the *Alpha* distribution of the  $\gamma$ -

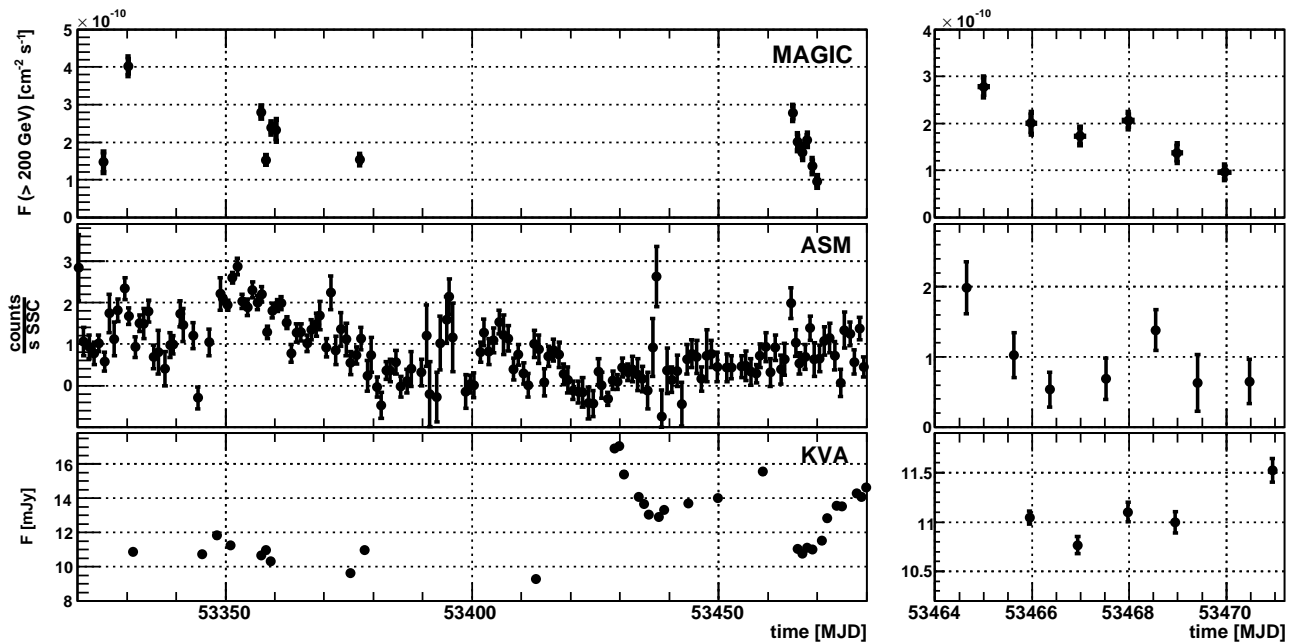


FIG. 5.— Night-by-night light curve for Mkn 421 from November 2004 to April 2005. *Left panels:* data from November 2004 to April 2005. *Right panels:* expanded data for 6 nights in April 2005. *Upper panel:* MAGIC data, night average of Mkn 421 above 200 GeV using samples I+III+IV. *Middle panel:* corresponding day-by-day X-ray counts as observed by the RXTE/ASM. *Lower panel:* Light curve of the optical flux of Mkn 421 as measured by the KVA telescope.

candidates of the combined samples I, II, and III with an energy threshold of  $\sim 150$  GeV. An excess of about 7000 events was found, which, for the given background, corresponds to an excess of more than 49 standard deviations. The number of excess events and the significances for the individual samples are summarized in Table 1.

Fig. 3 shows a sky map produced with the *Disp* method using samples III and IV. The reconstructed source position from the sky map (Fig. 3, indicated by the black cross) is centered at RA=+11h04'19", DEC=38°11'41". The systematic error of the telescope pointing is 2'. The  $\gamma$  PSF is indicated by a white circle in the left bottom corner. The observed extension of Mkn 421 is compatible with the MC expectation of a point source, which can also be seen in Fig. 2.

### 3.2. The light curve

The integral fluxes above 200 GeV, averaged over each night of observation, are shown in the upper panels of Fig. 5. Significant variations of up to a factor of four overall and up to a factor two in between successive nights can be seen. Since sample II has an energy threshold of 260 GeV it is not shown on the light curve. The relatively high analysis energy threshold of 200 GeV applied for the light curve ensures that the results are independent of the actual trigger thresholds during each night. In the middle panels of Fig. 5 the corresponding flux in the X-ray band as observed by the All-Sky-Monitor (ASM<sup>23</sup>) onboard the RXTE satellite is shown. In the lower panels of Fig. 5 the optical data taken by the KVA telescope<sup>24</sup> on La Palma are shown. Note that the contribution of the host galaxy (appr. 8.0 mJy) has been subtracted. While the X-ray data show a moderate variability within the observation period, the optical flux stays almost con-

stant.

For the 6 nights in April (MJD 53465 to 53471), the light curve above 200 GeV is shown in Fig. 6 in bins of 10 minutes. We also added the background rates for each night in the same binning, in order to demonstrate that the small variations in the excess rates and the daily changes are not caused by detector effects or atmospheric transmission changes. The vertical lines indicate the time in each night at which the observation mode was changed from ON to Wobble. The mean integral flux per night  $\bar{R}$  in units of  $10^{-9} \text{cm}^{-2} \text{s}^{-1}$  and the quality of the fit constant are shown in the panels. The horizontal dashed line corresponds to the integral flux of the Crab Nebula above 200 GeV. Combining the findings from the intra-night light curves we conclude that we did not find significant short-term flux variability within individual nights, despite the high sensitivity of MAGIC for such a search. Some of the nights, however, are less compatible with a constant flux than others, which might be an indication of some activity, albeit unstructured and difficult to quantify. On the other hand, we observe significant day-to-day variation by up to a factor of two, and differences up to a factor of four in the full sample.

### 3.3. The energy spectrum

#### 3.3.1. The measured spectrum

For the spectrum calculation, we combined the entire data set because the differences between the fluxes on individual nights are rather moderate (see Fig. 5). The resulting averaged differential energy spectrum is shown in Table 2 and in Fig. 7 by filled grey boxes. The energy spectra extend from around 100 GeV to several TeV. The last spectral point at 4.4 TeV is an 95% upper limit. The error bars shown are statistical only. Systematic errors are estimated to be 18% on the absolute energy scale, which correspond to 44% on the absolute flux level for a

<sup>23</sup> see [http://heasarc.gsfc.nasa.gov/xte\\_weather/](http://heasarc.gsfc.nasa.gov/xte_weather/)

<sup>24</sup> see <http://tur3.tur.iac.es/>

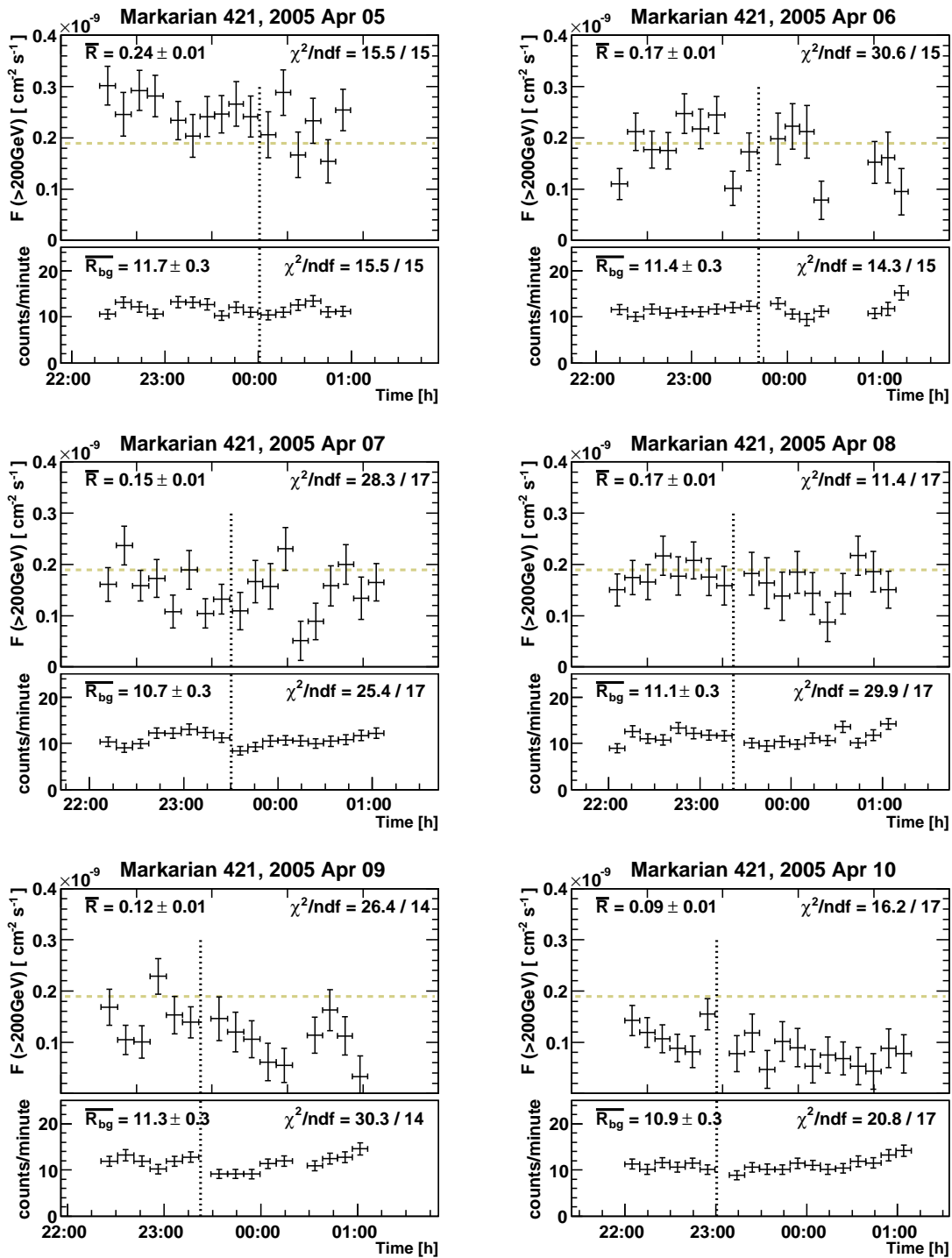


FIG. 6.— Light curve for 6 nights in 2006 April in 10 minutes binning. *Upper panels:* flux above 200 GeV. Mean rate  $\bar{R}$  in units of  $(10^{-9} \text{ cm}^{-2} \text{ s}^{-1})$  and the quality of the fit by a constant are shown in the panel. *Lower panels:* mean background rate  $\bar{R}_{\text{bg}}$  per minute after cuts. Note the rising background rate towards the end of each observation slot, related to the rising moon.  $\bar{R}_{\text{bg}}$  and the quality of the fit by a constant are shown. The vertical dotted lines indicate the time of the switchover from the ON observational mode to the Wobble mode. The dotted horizontal line indicates the Crab Nebula integral flux above 200 GeV as measured by MAGIC (Wagner et al. 2005).

photon index of 2.2. The systematic error on the slope is estimated to be 0.2. The attenuation of the VHE photons by intergalactic low energy photons and the determination of the intrinsic spectrum of Mkn 421 are discussed below.

### 3.3.2. $\gamma$ -ray absorption by the EBL

The VHE photons from Mkn 421 cross  $\sim 400$  million light years on their way to Earth. They interact with the low energy photons of the extragalactic background light (EBL, see Nikishov (1962); Gould & Schröder (1966); Stecker et al. (1992); Hauser & Dwek (2001)) consisting of redshifted star light of all epochs and reemission of a part of this light by dust in galaxies. The most common reaction channel between VHE  $\gamma$ -rays and the low energy photons of the EBL is pair production  $\gamma_{\text{VHE}} + \gamma_{\text{EBL}} \rightarrow e^+ e^-$ , a reaction which has its largest cross section when the center of mass energy is roughly 3.6 times larger than the threshold energy of  $2m_e c$ . The intrinsic (de-absorbed) photon spectrum,  $dN/dE_i$ , of a blazar located at redshift  $z$  is given by:

$$dN/dE_i = dN/dE_{\text{obs}} \times \exp[\tau_{\gamma\gamma}(E, z)],$$

where  $dN/dE_{\text{obs}}$  is the observed spectrum and  $\tau_{\gamma\gamma}(E, z)$  is the optical depth. The distance to Mkn 421 implies that the optical depth (e.g. Eq. 2 in Dwek & Krennrich (2005)) strongly depends on the shape and absolute photon density of the EBL between 1 and 30  $\mu\text{m}$  wavelength. A rather complicated distortion of the intrinsic spectrum takes place above  $\sim 100$  GeV. Although the calculation of the optical depth is straightforward, the spectral energy distribution of the EBL is uncertain. Direct measurements of the EBL are difficult because of the strong foreground emission consisting of reflected sunlight and thermal emission from zodiacal dust particles. Hence, many measurements lead to upper limits (Hauser et al. 1998; Dwek & Arendt 1998). Several measurements claimed a direct detection of the EBL, but some of them are controversial (Matsumoto et al. 2005; Finkbeiner et al. 2000). An alternative method to determine the EBL are fluctuation analyses of the measured radiation. Since a part of the EBL originates from discrete sources, fluctuations in the number of sources in an observer's field of view will produce fluctuations in the measured background (Kashlinsky et al. 1996; Kashlinsky & Odenwald 2000). A third method is the galaxy number counting in the deep field surveys, which provides robust lower limits to the SED of the EBL (Elbaz et al. 2002; Metcalfe et al. 2003; Fazio et al. 2004; Madau & Pozzetti 2000). The results of these methods and measurements are summarized in Fig. 8.

In principle, upper limits on the EBL can also be determined from observed  $\gamma$ -ray spectra from medium to high redshift TeV blazars. Under assumptions that the reconstructed TeV blazar spectrum is not too hard and it does not have a pile-up at high energies, the EBL level can be constrained (see Hauser & Dwek (2001) for summary and Aharonian et al. (2006) for latest results). However, since the measured spectrum of Mkn 421 is much softer than the one of Mkn 501, which is located at similar redshift, the softness seems to be intrinsic. In addition, the data in this paper extend up to 3 TeV only (historical data of Mkn 421 extend up to 20 TeV), which further weakens possible constraints from such a nearby

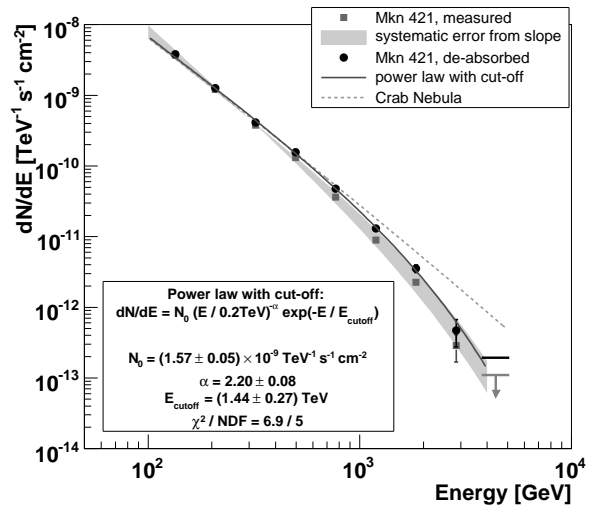


FIG. 7.— Differential energy distribution for Mkn 421 averaged over the whole data sample. The measured energy spectrum is shown by the grey full squares and the de-absorbed spectrum by the black full circles. The spectral point at the highest energy is a 95% upper limit. The grey shaded area corresponds to a systematic error from a slope error of  $\pm 0.2$  as quoted in the text. The black solid line indicates the best fit to the de-absorbed spectrum by a power law with exponential cut-off; its parameters are listed in the inset. For comparison reasons, the measured Crab Nebula spectrum (Wagner et al. 2005) is shown by the grey dotted line.

TABLE 2  
AVERAGED MEASURED DIFFERENTIAL ENERGY SPECTRUM OF MKN 421, DERIVED FROM THE DATA SET PRESENTED IN THE PAPER. THE LAST POINT IS AN 95% UPPER LIMIT.

energy bin [GeV]			differential flux $dN/dE$
lower bin limit	mean energy	upper bin limit	[photons / (TeV cm <sup>2</sup> s)]
108	134	167	$(3.72 \pm 0.34) \times 10^{-9}$
167	208	259	$(1.21 \pm 0.04) \times 10^{-9}$
259	321	402	$(3.77 \pm 0.15) \times 10^{-10}$
402	498	623	$(1.32 \pm 0.05) \times 10^{-10}$
623	770	965	$(3.63 \pm 0.19) \times 10^{-11}$
965	1192	1497	$(8.95 \pm 0.71) \times 10^{-12}$
1497	1845	2321	$(2.26 \pm 0.27) \times 10^{-12}$
2321	2856	3598	$(2.88 \pm 1.20) \times 10^{-13}$
3598	4429	5579	$< 1.10 \times 10^{-13}$

source. We therefore do not try to constrain EBL using this Mkn 421 data set.

Instead, we adopt the recent model of Primack et al. (2005), scaled up by a factor 1.5 (which is within the model uncertainties), to match lower limits set by the *Spitzer* mission and ISOCAM in the range of 4 to 15  $\mu\text{m}$  (Fazio et al. 2004; Elbaz et al. 2002; Metcalfe et al. 2003). The resulting EBL spectrum is shown in Fig. 8 by the black curve. This EBL spectrum agrees with alternative models (e.g. Kneiske et al. (2004); Pei et al. (1999); Blain et al. (1999); Stecker et al. (2006)) which are designed to predict the EBL today. It is also very close to the upper limits inferred from arguments on AGN spectra (Aharonian et al. 2006). Using this EBL spec-

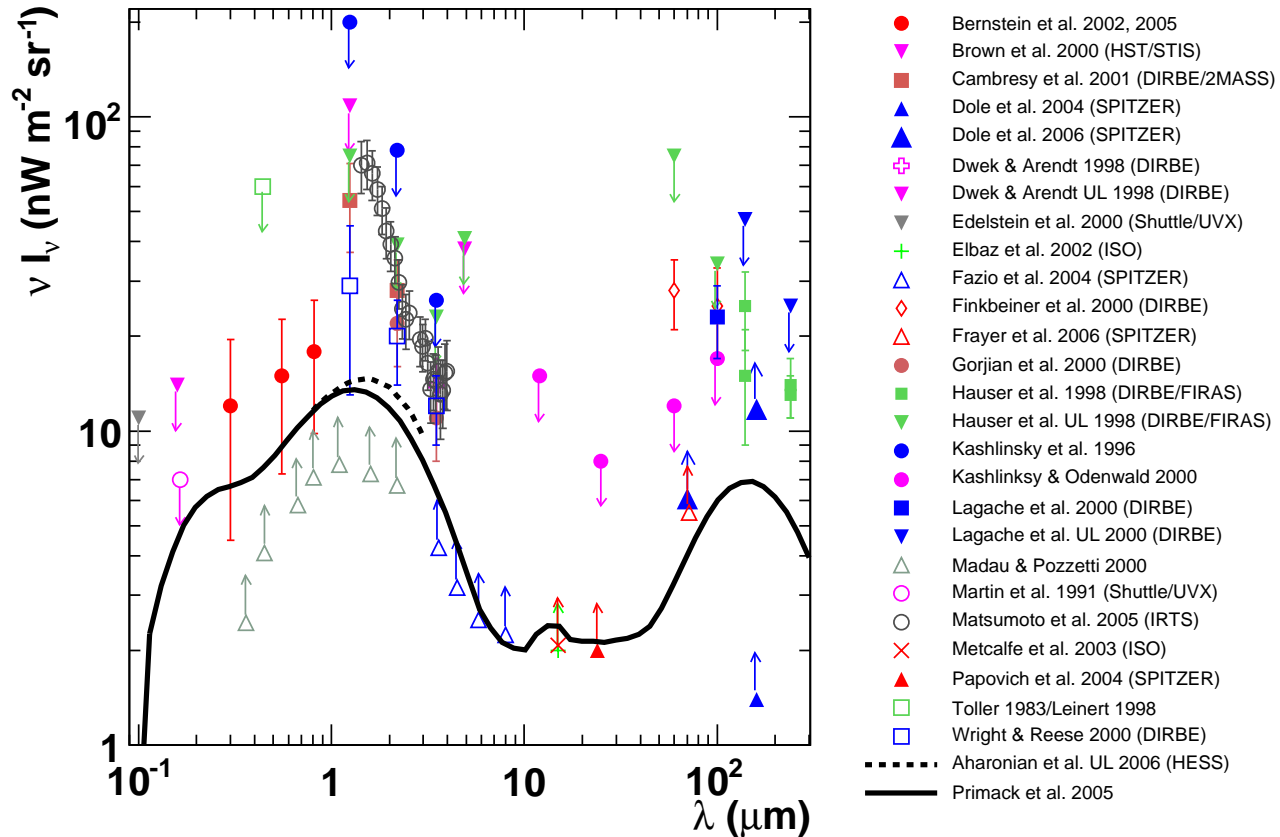


FIG. 8.— Energy density of the extragalactic background light (EBL). Direct measurements, galaxy counts, low and upper limits are shown by different symbols as described in the legend. The black solid curve is the EBL spectrum as in Primack et al. (2005) but upscaled by a factor 1.5 to match low limits derived from the galaxy counts (Elbaz et al. 2002; Metcalfe et al. 2003; Fazio et al. 2004).

TABLE 3

SYSTEMATIC STUDY OF THE FIT PARAMETERS ON THE DE-ABSORBED SPECTRUM OF Mkn 421. THE FITTED FUNCTION IS A POWER LAW WITH AN EXPONENTIAL CUT-OFF:

$dN/dE = N_0(E/0.2 \text{ TeV})^{-\alpha} \exp(-E/E_{\text{cutoff}})$ . WE SHOW FIT VALUES ON THE PHOTON INDEX,  $\alpha$ , AND THE CUT-OFF ENERGY,  $E_{\text{cutoff}}$ , FOR FOLLOWING ASSUMPTIONS: NOMINAL VALUES (A), A SYSTEMATIC SHIFT BY +18% IN THE VHE ENERGY SCALE (B), A SYSTEMATIC SHIFT BY -18% IN THE VHE ENERGY SCALE (C), A SYSTEMATIC SHIFT BY +18% IN THE VHE ENERGY SCALE AND, IN ADDITION, 25% MORE DENSITY OF THE EBL (D), AND A SYSTEMATIC SHIFT BY -18% IN THE VHE ENERGY SCALE AND, IN ADDITION, 25% LESS DENSITY OF THE EBL (E). NOTE THAT THE RESULTING SYSTEMATIC ERRORS ARE COMPARABLE WITH THE STATISTICAL ERRORS.

	$\alpha$	$E_{\text{cutoff}}$ [TeV]
A: nominal	$2.20 \pm 0.08$	$1.44 \pm 0.28$
B: E+18%	$2.16 \pm 0.08$	$1.59 \pm 0.29$
C: E-18%	$2.24 \pm 0.08$	$1.26 \pm 0.26$
D: (E+18%) + (EBL+25%)	$2.12 \pm 0.08$	$1.61 \pm 0.29$
E: (E-18%) + (EBL-25%)	$2.20 \pm 0.08$	$1.09 \pm 0.20$

spectrum and state-of-the-art cosmology (flat universe, Hubble constant  $H_0=72 \text{ km/s/Mpc}$ , matter density  $\Omega_m=0.3$ , dark energy density  $\Omega_\Lambda=0.7$ ) we calculated the optical depth  $\tau_{\gamma\gamma}$  for Mkn 421. Thereby we use numerical integration of Eq. 2 from Dwek & Krennrich (2005). The

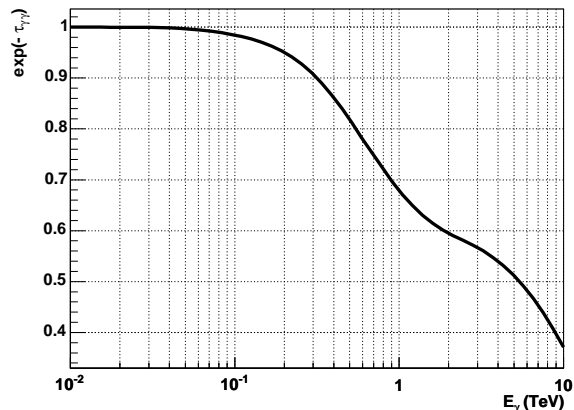


FIG. 9.— Attenuation coefficient  $\exp(-\tau_{\gamma\gamma})$  for Mkn 421 ( $z=0.030$ ) using the EBL spectrum as shown in Fig. 8.

attenuation coefficients  $\exp(-\tau_{\gamma\gamma})$  are shown as the function of energy of VHE  $\gamma$ -rays in Fig. 9. We note that the attenuation coefficients are very similar to those from Stecker et al. (2006).

### 3.3.3. The de-absorbed spectrum of Mkn 421

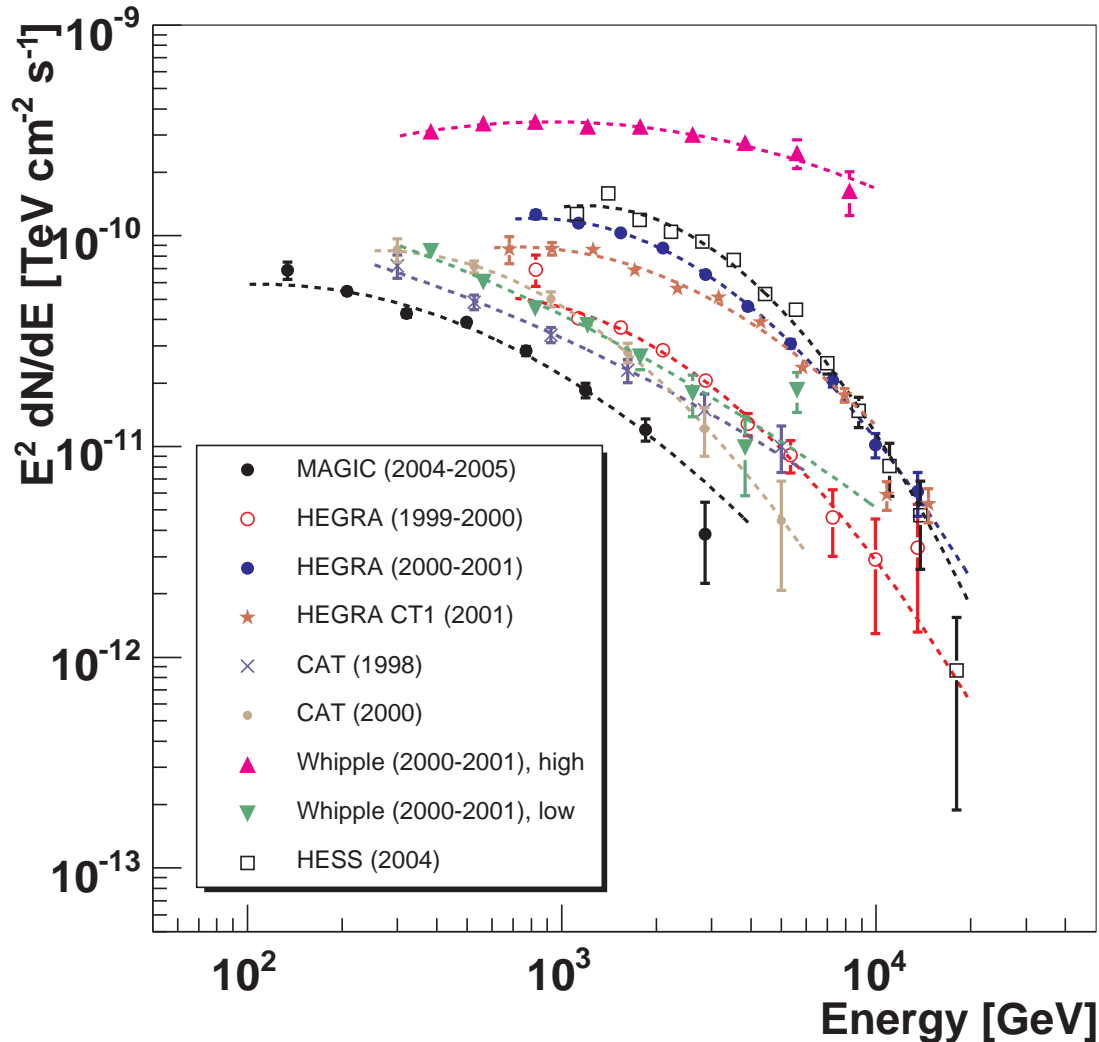


FIG. 10.— Differential energy spectra of Mkn 421 multiplied by  $E^2$  in different activity states from different experiments. The spectra are de-absorbed using the EBL model from Primack et al. (2005), upscaled by a factor of 1.5. A log-parabolic fit is performed (dashed lines) to determine the peak position in the SED (see Fig. 12). For clarity, only the highest and lowest of the published Whipple results are shown. Note that for the MAGIC spectrum the upper limit at 4.4 TeV is not plotted.

The measured spectrum and the reconstructed de-absorbed (i.e. corrected for the effect of intergalactic absorption) spectrum are shown in Fig. 7. For comparison reasons, the Crab Nebula spectrum is also shown. The de-absorbed spectrum (shown by filled black circles) is clearly curved, its probability of being a simple power law is  $1.6 \times 10^{-8}$ . The de-absorbed spectrum is fitted by a power law with an exponential cut-off:  $dN/dE = N_0(E/0.2 \text{ TeV})^{-\alpha} \exp(-E/E_{\text{cutoff}})$ ,  $\alpha$  being the photon index, solid line in Fig. 7. The fit parameters are listed in the inlay of Fig. 7. The power law with a cut-off describes well the de-absorbed spectrum of Mkn 421, with a photon index  $\alpha = 2.20 \pm 0.08$  and a cut-off energy of  $E_{\text{cutoff}} = (1.44 \pm 0.28) \text{ TeV}$ . Taking into account the systematic uncertainty of 18% on the absolute energy scale of our measurement and in addition a guessed 25% uncertainty on the EBL level, we find that neither the

photon index nor the cut-off energy substantially change (See Table 3). The fitted photon index was found to be between 2.12 and 2.24, whereas the cut-off energy was found to be between 1.1 and 1.6 TeV. From this study we conclude that the curvature of the spectrum is source inherent: either at the measured flux level this cosmic accelerator is close to its energy limit, or there exists a source-intrinsic absorption.

## 4. DISCUSSION

### 4.1. Comparison with previous observations of Mkn 421

In Fig. 10 we show the (de-absorbed) energy density spectrum in context with several previously published high statistics observations of Mkn 421. For a compilation of the VHE measurements of Mkn 421 we used historical data from CAT (Piron et al. 2001),

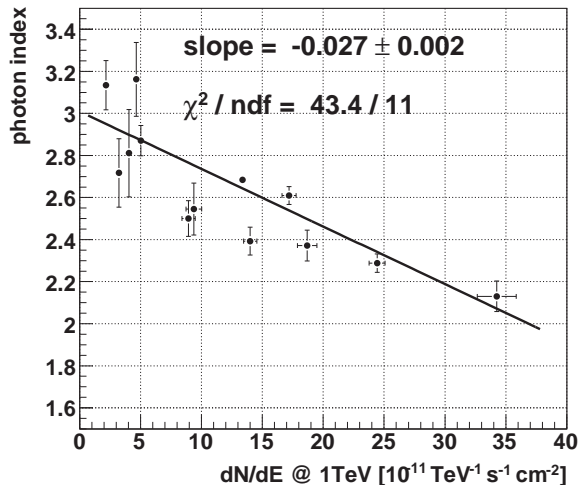


FIG. 11.— Relation between the flux state at 1 TeV (determined from a power law approximation of the spectra between 700 GeV and 4 TeV) and the fitted photon index of published data as in Fig. 10. A correlation between flux and hardness can be clearly seen.

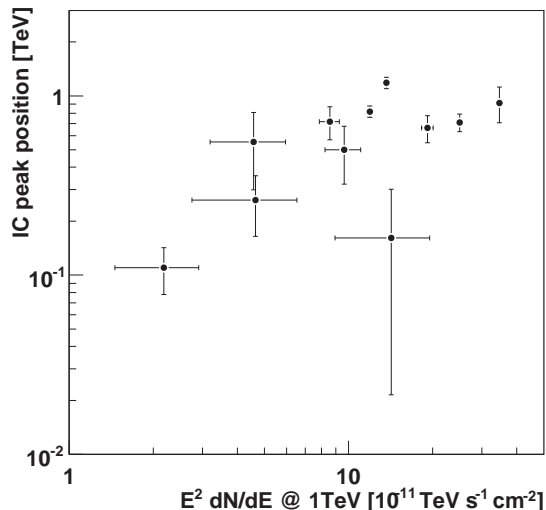


FIG. 12.— Relation between the fitted peak position in the SED and the energy density at 1 TeV for published data as in Fig. 10. A clear trend can be observed for the peak position to shift towards higher energies with increased source intensity.

HEGRA (Aharonian et al. 2002; Schweizer 2002), HESS (Aharonian et al. 2005), and Whipple (Krennrich et al. 2002)<sup>25</sup>. All measured spectra are de-absorbed using the EBL model as described in Subsection 3.3.2. The activity of the source during MAGIC observations clearly was at the lower end, and our results extend to energies lower than those previously observed, thus being complementary both in source intensity and energy range.

<sup>25</sup> For the Whipple measurements, only spectra in the highest and in the lowest flux state are shown in order not to clutter Fig. 10

All results seem consistent with each other, and all show significant deviations from a simple power law, which can not be explained by attenuation effects (the results are robust with respect to the EBL model within a factor  $\pm 25\%$ ). They are, therefore, likely to be source-intrinsic.

From the compilation of the de-absorbed Mkn 421 spectra, it is evident that with an increasing flux state the spectrum becomes harder. In order to verify this, we fitted the spectra by a simple power law ( $dN/dE \propto E^{-\alpha}$ ) in the overlapping energy region between 700 GeV and 4 TeV. The resulting photon indices  $\alpha$  as function of the fitted flux at 1 TeV are shown in Fig. 11. Evidently, with increasing flux the spectra harden. Similar results were obtained using Whipple data (Krennrich et al. 2002), HEGRA data (Aharonian et al. 2002, 2003), and CAT data (Giebels et al. 2006).

The curvatures observed are indicative of a maximum in energy density, and are usually interpreted as due to inverse-Compton (IC) scattering. The peak position appears to be dependent on the source flux intensity. We have, therefore, performed a log-parabolic fit for all available data. The log-parabola has the following parametrization:  $\log_{10}(\nu F_{\nu}) = A + B(\log_{10}(E) - \log_{10}(E_p))$ , with  $\nu F_{\nu} = E^2 dN/dE$  and  $E_p$  being the energy of the peak position. The best log-parabolic fits are shown in Fig. 10 by the dashed lines. In Fig. 12 we compare the resulting peak positions for the different experiments as a function of their (fitted) energy density at 1 TeV. Evidently, with increasing flux the peak shifts to higher energy values. Future observations at higher intensities extending to lower energies will have to corroborate these results. Such observations are part of the future MAGIC physics programme.

#### 4.2. A short comment on the light curves

In the observation period between November 2004 and April 2005 we observed night-to-night flux variations up to a factor of 2 and a maximum flux change in the entire set of a factor 4. No short-term flux variations well below 1 hour, as observed during high flaring activity in previous experiments (Gaidos et al. 1996; Aharonian et al. 2002), were seen, although the sensitivity of MAGIC would allow to detect fast flares in the given flux range. Two equally likely explanations are that either we deal with large fluctuations resulting in the absence of any fast flare during the observation period, or fast flaring is a feature that occurs only when the source is very active. This calls for further high statistics and high sensitivity studies when the source is in its low flux state.

#### 4.3. Correlation studies

The correlation between the  $\gamma$ -ray flux measured by MAGIC and the X-ray flux measured by RXTE/ASM is shown in Fig. 13. For the MAGIC flux we take the nightly average above 200 GeV (see also Fig. 5). For the X-ray data, we calculate the average of those RXTE/ASM pointings (dwells) which were taken simultaneously with MAGIC data, allowing  $\pm 1$  hour with respect to the MAGIC data, to increase X-ray statistics. Fig. 13 shows a clear correlation between X-ray and  $\gamma$ -ray data. The linear fit (solid line), forced to go through (0,0), has a slope of  $1.4 \pm 0.1 [ \frac{10^{-10}}{\text{cm}^2} / \frac{\text{counts}}{\text{SSC}} ]$ , and has a  $\chi^2$  probability of 54%. The parabolic fit (dashed line) which

## 4.4. Comparison with models

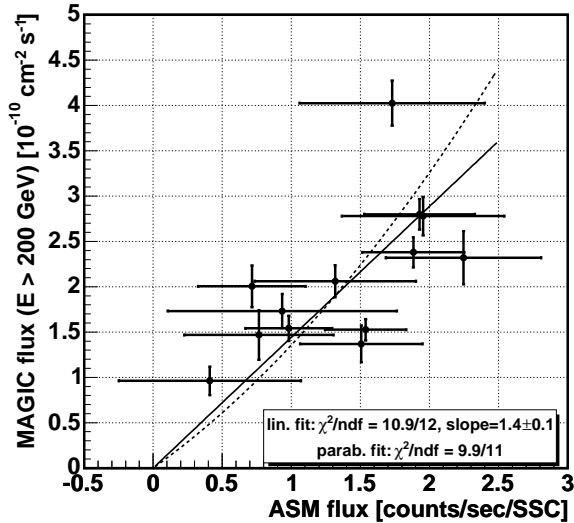


FIG. 13.— Correlation between MAGIC integral flux measurements above 200 GeV and RXTE/ASM counts for 13 nights.

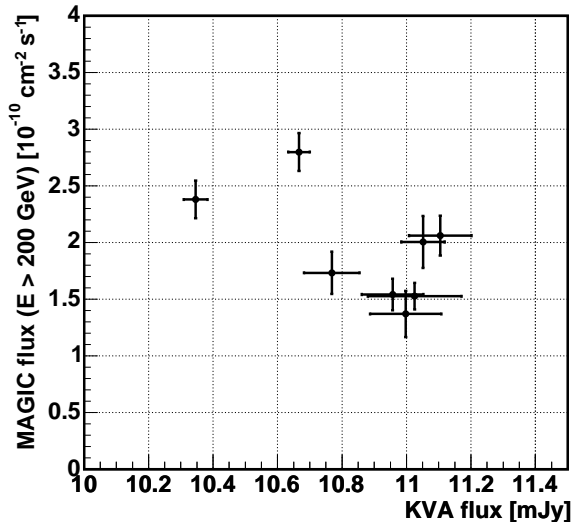


FIG. 14.— Correlation between MAGIC integral flux above 200 GeV and optical flux measured by the KVA telescope for 8 nights.

is also forced to go through (0,0) has the same  $\chi^2$  probability of 54%. The correlation coefficient  $r = 0.64^{+0.15}_{-0.22}$  (errors correspond to  $1\sigma$  level) is different from zero by 2.4 standard deviations (taking into account the non-linearity of errors).

In Fig. 14 the MAGIC  $\gamma$ -ray flux above 200 GeV is shown together with simultaneous KVA optical data. The latter have been averaged over the MAGIC integration time. One can see a possible  $\gamma$ -ray/optical anti-correlation during the 8 nights of simultaneous observations, however, the correlation coefficient  $r = -0.59^{+0.36}_{-0.22}$  is compatible with zero within 1.5 standard deviations.

Given the temporal correlation between X-ray and  $\gamma$ -ray fluxes, it is reasonable to infer that the VHE  $\gamma$ -ray radiation is dominated by emission resulting from IC upscattering of the synchrotron X-ray photons by their parent population of relativistic electrons. Such correlation can be modelled with a homogeneous synchrotron-self-Compton (SSC) model. Based on this model it is possible to constrain the parameter space of the emission region and estimate its basic parameters, the Doppler factor,  $D$ , and the rest-frame magnetic field,  $B$ , of the emitting plasma in the relativistic jet. To this end we follow the procedure first devised by Bednarek & Protheroe (1997) for the Mkn 421 flare of 16 May 1994, subsequently improved by, e.g., Tavecchio et al. (1998); Bednarek & Protheroe (1999); Kataoka et al. (1999); Katarzynski et al. (2003). Application of this method requires precise simultaneous multiwavelength information. Since a synchrotron (X-ray) spectrum simultaneous with the MAGIC observations is not available, we have to resort to previous X-ray observations arguing that similar TeV  $\gamma$ -ray states (IC emission) should correspond to similar X-ray states (synchrotron emission). In fact, similar  $\gamma$ -ray spectra of Mkn 421 have already been observed several times – including the HEGRA observations in April 1998 (Aharonian et al. 1999) for which simultaneous *BeppoSAX* observations are available (Fossati et al. 2000; Massaro et al. 2004). Here we use the X-ray spectra and parameterization, reported by Massaro et al. (2004) for 21 April 1998. It is also noticeable that the X-ray flux level between the simultaneous RXTE/ASM data and the *BeppoSAX* data used here is very similar (see Fig. 16).

The low flux state MAGIC  $\gamma$ -ray spectrum, reported here for energies at  $\sim 100$  GeV, warrants a better investigation of the crucial energy range where the IC peak is expected to occur, than in previous data sets. Following Bednarek & Protheroe (1997, 1999) we then constrain the allowed parameters of the emission region ( $D$  and  $B$ ) from the ratio of the  $\gamma$ -ray power to the X-ray power, measured at their respective peak emission (see thick curves in the upper panels of Fig. 15). The radiation field density and the electron spectrum, cospatial in the blob, were derived as a function of  $D$  and  $B$  for a blob radius assumed equal to the light travel corresponding to the shortest reported variability time scale (for observational arguments see Takahashi et al. (2000)). We further constrain the allowed parameter space by arguing that the synchrotron and IC cooling time scales should be shorter than the observed variability time scale. These conditions are fulfilled above the dot-dashed lines (for synchrotron cooling) and on the left of the grey dashed line (for the IC cooling) for the 1 hr (upper left panel of Fig. 15) and 1 day (upper right panel of Fig. 15) variability time scales. The condition that the blob has to be transparent to the VHE  $\gamma$ -rays leads to a further lower bound on  $D$  by requiring that the optical depth by pair production has to be lower than unity. The corresponding limits for photon energies of 100 GeV and 3 TeV (which define the energy range of MAGIC measurement) are shown in the upper panels of Fig. 15 as thin and thick dotted lines, respectively. One last

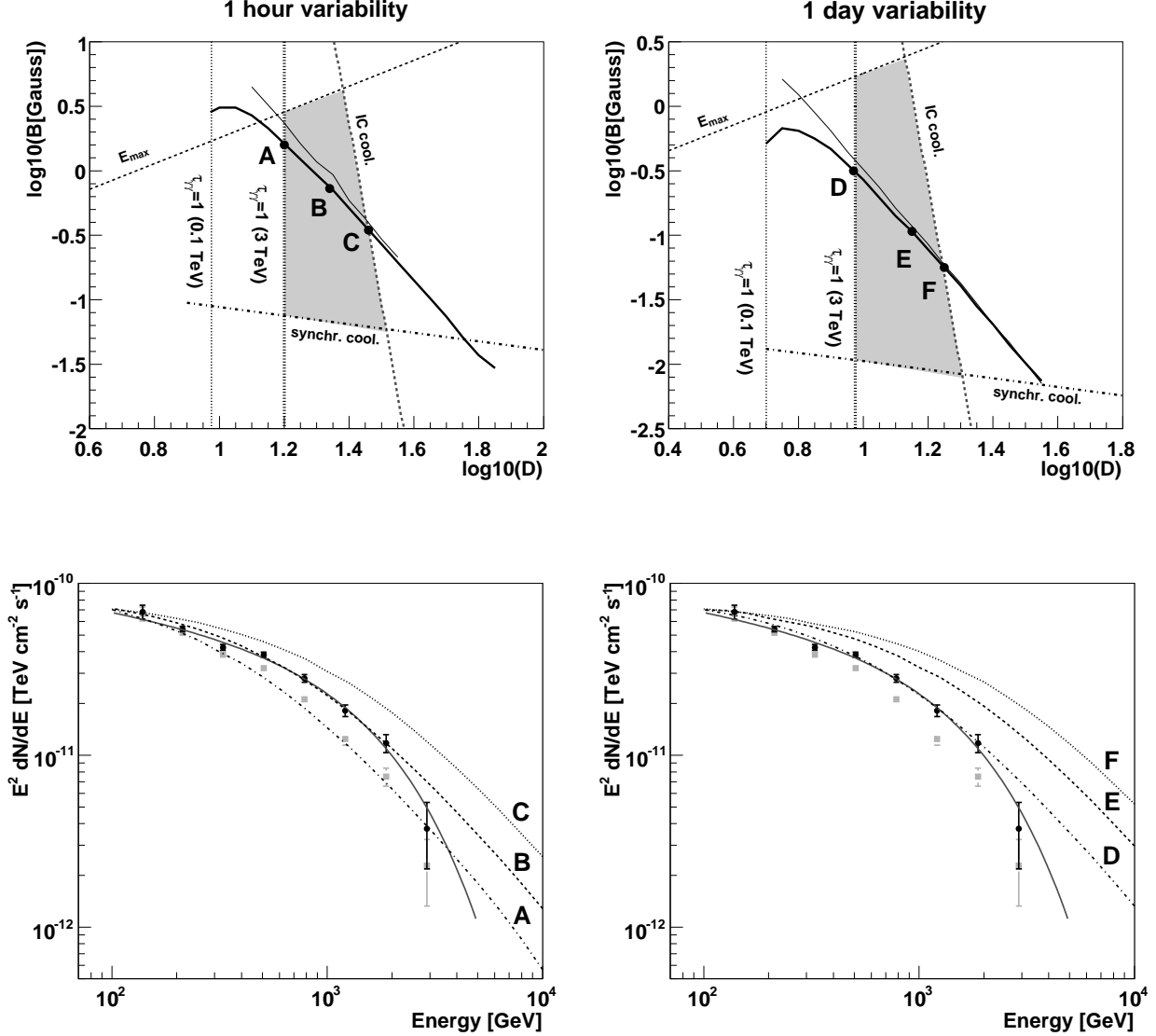


FIG. 15.— Constraints on the parameter space (Doppler factor,  $D$ , versus magnetic field strength,  $B$ ) for the emission region in the jet of Mkn 421 based on the one-zone homogeneous SSC model. From the ratio of the  $\gamma$ -ray to X-ray power during the MAGIC observations of Mkn 421 (measured at the peaks in the synchrotron and IC spectra) the allowed values are limited to the thick curves (assumed IC peak at 100 GeV) or to the thin curves (assumed IC peak at 10 GeV). The left figures correspond to a 1 hour variability, whereas the right figures correspond to a 1 day variability. The physical conditions in the blob are limited by the electron cooling on the synchrotron and IC processes, optical depth for  $\gamma$ -rays, and maximum energy of electrons as discussed in the text. These constraints are shown by the dashed and dot-dashed lines. The allowed region is limited by these lines and is marked by the grey shaded area. The  $\gamma$ -ray spectra are calculated for the values of the Doppler factor and magnetic field strength marked by A, B, and C (for 1 hr variability), and D, E, and F (for 1 day variability). They are compared with the de-absorbed MAGIC spectrum (shown as full black circles) in the bottom figures. The fit by a power law with an exponential cut-off to the de-absorbed spectrum (as in Fig 7) is shown by the black solid line, whereas the measured spectrum is shown by the grey full squares.

condition arises from comparing the maximum energy of electrons, determined by the maximum energy of synchrotron photons  $\sim 40$  keV, with the maximum energy of the detected photons  $\sim 3$  TeV (see dashed line in the upper panels of Fig. 15). These limiting conditions build an allowed region in the  $D$ - $B$  plane as marked by the grey shaded area. The allowed parameters of the emission region correspond to the part of the thick full curve inside the region limited by all these lines (see Fig. 15). In order to determine the values of  $D$  and  $B$  more precisely, we now calculate the  $\gamma$ -ray spectra for the points A, B, and C for 1 hr variability, and the points D, E, and

F for 1 day variability, and compare the predicted spectrum with the actual de-absorbed spectrum. From the lower panels of Fig. 15 it is clear that the best description is provided by the blob with Doppler factor  $D \sim 22$  and magnetic field  $B \sim 0.7$  G (the point B) for 1 hr variability, and  $D \sim 9$  and  $B \sim 0.3$  G (the point D) for 1 day variability. In order to assess how this result is sensitive on the correct energy localization of the peak in the  $\gamma$ -ray spectrum (which is in fact only limited by the lower energy end of the MAGIC spectrum), we show the allowed parameter space for the  $\gamma$ -ray peak at 10 GeV (see thin full curves in Fig. 15). The constraints for the

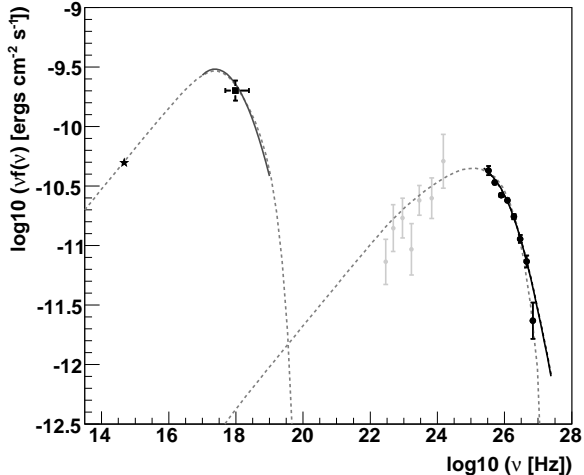


FIG. 16.— The overall SED of Mkn 421 from optical wavelengths through VHE  $\gamma$ -rays. Large symbols represent averaged data described in this paper: optical data from KVA (star), X-rays from RXTE/ASM (full square), de-absorbed  $\gamma$ -rays from MAGIC (full points). The grey full squares are archival EGRET measurements (Hartman et al. 1999). The grey curve in the X-rays corresponds to the log-parabolic fit taken from Massaro et al. (2004) using *BeppoSAX* (Boella 1997) data of Mkn 421 taken on 21 April 1998. The two black curves through the  $\gamma$ -ray spectrum (almost indistinguishable) correspond to the SSC model parameter sets B and D (see text and Fig. 15 for details). The grey dashed line denotes a fit by the SSC model as in Krawczynski et al. (2004), see text for details.

peak at 10 GeV and 100 GeV are almost the same for the parts of the curves inside the allowed region. It is interesting that the emission parameters, as estimated here for the low flux state of Mkn 421 (for the 1 day variability time scale), are not very different from those estimated by Bednarek & Protheroe (1997) for the flaring state. This suggest that the flaring state may not be related to the significant change of the blob’s Doppler factor and magnetic field strength.

In Fig. 16 we show the broadband SED of Mkn 421. Large symbols represent averaged data described in this paper: optical data from KVA (star), X-rays from RXTE/ASM (full square),  $\gamma$ -rays from MAGIC (full points). The grey curve in the X-rays corresponds to a log-parabolic fit performed by Massaro et al. (2004) on *BeppoSAX* data of Mkn 421 taken on 21 April 1998. The two black curves through the  $\gamma$ -ray spectrum are almost indistinguishable and correspond to the best SSC model parameters for 1-hr and 1-day variability time scales (points B and D respectively, calculated according to Eq. (13) in Bednarek & Protheroe (1999) who apply the Klein-Nishina cross-section as in 2.48 of Blumenthal & Gould (1970)).

In addition, we apply the SSC code provided by Krawczynski et al. (2004) to our dataset. The fitted overall SED is shown by the grey dashed line in Fig. 16, and the model parameters are listed in Table 4. For the fit, we used the simultaneous KVA, ASM and MAGIC data, as well as the archival *BeppoSAX* observations from 21 April 1998 (Massaro et al. 2004). In contrast to the parameters adopted in Krawczynski et al. (2001), we used a smaller Doppler factor (15 instead of 50), result-

TABLE 4  
SSC MODEL PARAMETERS FOR MKN 421. THE CORRESPONDING PHOTON SPECTRUM IS SHOWN IN FIG. 16.

spherical blob with:	
Doppler factor	15
magnetic field	0.20 Gauss
radius of emitting region	$1.6 \times 10^{16}$ cm
injected electron spectrum:	
electron energy density	0.06 erg/cm <sup>3</sup>
$5 < \log_{10}(E[\text{eV}]) < 10.9$	index 2.31
$10.9 < \log_{10}(E[\text{eV}]) < 11.6$	index 3.88

ing in a somewhat larger emitting region ( $1.6 \times 10^{16}$  cm instead of  $2.7 \times 10^{15}$  cm), and a higher particle density (0.06 erg/cm<sup>3</sup> instead of 0.01 erg/cm<sup>3</sup>). We note that the fitted values of magnetic field and Doppler factor are within the allowed range as defined above. Remarkably, the archival EGRET data (Hartman et al. 1999) matches the fit almost perfectly, suggesting an IC peak around 100 GeV.

## 5. CONCLUDING REMARKS

Mkn 421 was observed with the MAGIC telescope during several months in 2004 and 2005. Briefly, we have presented the following:

- first high-sensitivity observation down to  $\approx 100$  GeV;
- first observation of an IC peak at low flux;
- absence of short flares below 1 hour duration despite sufficient sensitivity;
- flux variation up to a factor 2 between consecutive nights and up to a factor 4 in the entire observation period;
- confirmation of a source-inherent effect resulting in a curved spectrum after de-absorption (for reasonable assumptions concerning the EBL) in case of low flux intensity;
- a strong correlation between spectral hardness (photon index between 700 GeV and 4 TeV) and flux intensity, obtained by comparison of the de-absorbed energy spectra of various experiments covering different flux levels;
- a clear trend for the peak position to shift towards higher energies with increased source intensity, obtained by the same comparison;
- confirmation of a significant correlation between X-ray and VHE  $\gamma$ -ray intensity during a state of low to medium intensity;
- a hint that different flaring states result from differences in electron populations (electron spectrum) rather than from significant change of the blob’s Doppler factor and magnetic field strength.

We add the following conclusions. The flux state was found to be comparatively low, ranging in intensity between 0.5 and 2 Crab units when integrated above 200 GeV. While clear night to night variations were

found, the intra-night light curve, binned in 10-minute time intervals, does not show significant variations, although several nights are only marginally compatible with a constant flux. They do not show a discernible structure, though, and seem not associated to an overall flux different from that of perfectly quiescent nights. We note that MAGIC is sensitive enough to detect variabilities on the 10-minute time scale at such a low flux level. A clear correlation ( $r = 0.64_{-0.22}^{+0.15}$ ) between X-rays and  $\gamma$ -rays was found, while no correlation was seen between optical and  $\gamma$ -rays. This supports a leptonic origin of the  $\gamma$ -rays from Mkn 421. The energy spectrum resulting from the combined MAGIC data, corrected for the extragalactic absorption, suggests the presence of an IC peak at about 100 GeV. The spectrum is clearly curved at energies above 1 TeV, and can be fitted by a power-law with an exponential cut-off. The overall SED observed in the observed flux state can be well described by a homogeneous SSC model provided that the emission re-

gion moves with a Doppler factor  $\sim 9$  and its magnetic field strength is  $\sim 0.3$  G for a 1-day variability time scale. Surprisingly, these parameters do not differ substantially from those estimated for the emission region of Mkn 421 during a strong flare (Bednarek & Protheroe 1997). The fit with an alternative SSC code of Krawczynski et al. (2001) lead to similar Doppler factor and magnetic field values.

We would like to thank the IAC for the excellent working conditions at the Observatory de los Muchachos in La Palma. The support of the German BMBF and MPG, the Italian INFN and the Spanish CICYT is gratefully acknowledged. This work was also supported by ETH Research Grant TH 34/04 3 and the Polish MNiI Grant 1P03D01028. We also thank Dieter Horns and Frank Krennrich for providing us with HEGRA, H.E.S.S., and Whipple data.

## REFERENCES

- Aharonian, F. et al. (HEGRA Collab.), 1999, *A&A*, 350, 757.  
 Aharonian, F. et al. (HEGRA Collab.), 2002, *A&A*, 393, 89.  
 Aharonian, F. et al. (HEGRA Collab.), 2003, *A&A*, 410, 813.  
 Aharonian, F. et al. (HEGRA Collab.), 2004, *ApJ*, 614, 897.  
 Aharonian, F. et al. (H.E.S.S. Collab.), 2005, *A&A*, 437, 95.  
 Aharonian, F. et al. (H.E.S.S. Collab.), 2006, *Nature*, 440, 1018.  
 Anykeyev, V.B. et al., 1991, *Nucl. Instrum. Methods A*, 303, 350.  
 Bednarek, W., Protheroe, R.J., 1997, *MNRAS*, 292, 646.  
 Bednarek, W., Protheroe, R.J., 1999, *MNRAS*, 310, 577.  
 Bernstein, R. et al., 2002, *ApJ*, 571, 56,85,107.  
 Bernstein, R. et al., 2005, *ApJ*, 632, 713.  
 Bertero, M., *Advances in Electronics and Electron Physics*, Vol 75, Academic Press 1989.  
 Blain, A.W. et al., 1999, *MNRAS*, 309, 715.  
 Błażejowski, H. et al., 2005, *ApJ*, 630, 130.  
 Blumenthal, G.R. and Gould, R.J., *Rev. Mod. Phys.*, 42,237,1970.  
 Bock, R.K. et al., 2004, *Nucl. Instrum. Methods A*, 516, 511.  
 Boella, G. et al., 1997, *A&A*, 122, 299.  
 Breiman, L., 2001, *Machine Learning*, 45, 5  
 Bretz, T. (for the MAGIC Collab.), *AIP Conf. Proc.*, 2005, 745, 730.  
 Brown, T.M. et al., 2000, *Astronom. Journal*, 120, 1153  
 Cambresy, L. et al., 2001, *ApJ*, 555, 563.  
 Cortina, J. et al. (MAGIC Collab.), 2005, *Proc. 29th ICRC (Pune)*, 5, 359  
 Costamante, L. & Ghisellini, G., 2002, *A&A*, 384, 56.  
 Coppi, P.S., 1992, *MNRAS*, 258, 657.  
 Daum, A. et al. (HEGRA Collab.), 1997, *Astropart. Phys.*, 8, 1.  
 Dole, H. et al., 2004, *ApJSS*, 154, 87.  
 Dole, H. et al., 2006, *A&A*, 451, 417.  
 Domingo-Santamaría, E. et al. (MAGIC Collab.), 2005, *Proc. 29th ICRC (Pune)*, 5, 363  
 Dwek, E. & Arendt, R.G., 1998, *ApJ*, 508, L9.  
 Dwek, E. & Krennrich, F., 2005, *ApJ*, 618, 657.  
 Edelman, J., Bowyer, S., & Lampton, M., 2000, *ApJ*, 539, 187.  
 Elbaz, D. et al., 2002, *A&A*, 384, 848.  
 Fazio, G.G. & Stecker, F.W., 1970, *Nature* 226, 135  
 Fazio, G.G. et al., 2004, *ApJSS*, 154, 39.  
 Finkbeiner et al., 2000, *ApJ*, 544, 81.  
 Fomin, V. P. et al., 1994, *Astropart. Phys.*, 2, 137.  
 Fossati, G. et al., 2000, *ApJ*, 541, 166.  
 Frayer, D.T. et al., 2006, *Astronom. Journal*, 131, 250.  
 Gaidos, J. A. et al., 1996, *Nature*, 383, 319.  
 Gaug, M. et al. (MAGIC Collab.), 2005, *Proc. 29th ICRC (Pune)*, 5, 375  
 Giebels, B. et al., 2006, accepted by *A&A*, astro-ph/0610270  
 Gorjian, V. et al., 2000, *ApJ*, 536, 550.  
 Gould, R.J. & Schröder, 1966, *Phys. Rev. Lett.*, 16, 252.  
 Hartman, R.C. et al., 1999, *ApJSS*, 123, 79-202.  
 Hauser, M.G. et al., 1998, *ApJ*, 508, 25.  
 Hauser, M.G. & Dwek, E., 2001, *ARA&A*, 39, 249.  
 Hillas, A. M., 1985, *Proc. of the 19th ICRC, La Jolla*.  
 Hillas, A. M., et al., 1998, *ApJ*, 503, 744.  
 Kashlinsky, A. et al., 1996, *ApJ*, 470, 681.  
 Kashlinsky, A. & Odenwald, S., 2000, *ApJ*, 528, 74.  
 Kataoka, J. et al., 1999, *ApJ*, 514, 138.  
 Katarzyński, K., Sol, H., Kus, A., 2003, *A&A*, 410, 101.  
 Knapp, J. & Heck, D., 2004, *EAS Simulation with CORSIKA: A Users Manual*.  
 Kneiske, T. M. et al., 2004, *A&A*, 413, 807.  
 Krennrich, F. et al., 2002, *ApJ*, 575, L9.  
 Krawczynski, H. et al., 2001, *ApJ*, 559, 187.  
 Krawczynski, H. et al., 2004, *ApJ*, 601, 151.  
 Lagache, G. et al., 2000, *A&A*, 354, 247.  
 Lessard, R. W. et al., 2001, *Astropart. Phys.*, 15, 1.  
 Leinert, Ch. et al., 1998, *A&A*, 127, 1.  
 Lorenz, E., *New Astron. Rev.*, 2004, 48, 339.  
 Li and Ma, 1983, *ApJ*, 272, 317.  
 Mannheim, K. et al., 1996, *A&A*, 315, 77.  
 Madau, P. & Pozzetti, L., 2000, *MNRAS*, 312, L9.  
 Majumdar, P. et al., 2005, *Proc. 29th ICRC (Pune)*, 5, 203  
 Martin, C., 1991, *ApJ*, 379, 549.  
 Massaro, E., 2004, *A&A*, 413, 489.  
 Matsumoto, T. et al., 2005, *ApJ*, 626, 31.  
 Mazin, D. et al., 2005, *Proc. 29th ICRC (Pune)*, 4, 331  
 Metcalfe, L. et al., 2003, *A&A*, 407, 791.  
 Mücke, A. et al., 2003, *Astropart. Phys.*, 18, 593.  
 Nikishov, A.I., 1962, *Sov. Phys. JETP*, 14, 393.  
 Papovich, C. et al., 2004, *ApJSS*, 154, 70.  
 Pei, Y.C. et al., 1999, *ApJ*, 522, 604.  
 Petry, D. et al., 1996, *A&A*, 311, L13.  
 Piron, F., et al., 2001, *A&A*, 374, 895.  
 Primack, J. et al., *AIP Conf. Proc.*, 2005, 745, 23.  
 Punch, M. et al., 1992, *Nature*, 358, 477.  
 Schweizer, T., 2002, *PhD thesis, Barcelona*, available at [http://wwwmagic.mppmu.mpg.de/publications/theses/ThomasS\\_thesis.ps.gz](http://wwwmagic.mppmu.mpg.de/publications/theses/ThomasS_thesis.ps.gz)  
 Stecker, F.W., De Jager, O.C., Salamon, M.H., 1992, *ApJ*, 390, L49.  
 Stecker, F.W., Malkan, M.A., & Scully, S.T., 2006, *ApJ*, 648, 774.  
 Takahashi, T. et al., 2000, *ApJ*, 542, L105.  
 Tavecchio, F., Maraschi, L., Ghisellini, G., 1998, *ApJ*, 509, 608.  
 Toller, G.N., 1983, *ApJ*, 266, L79.  
 Wagner, R.M. et al. (MAGIC Collab.), 2005, *Proc. 29th ICRC (Pune)*, 4, 163  
 Wright, E.L. & Reese, E.D., 2000, *ApJ*, 545, 43.